Shear-induced migration of rigid spheres in a Couette flow

Guillaume Ovarlez, Elisabeth Guazzelli

Shear-induced migration of rigid spheres in a Couette flow

Guillaume Ovarlez[1] and Élisabeth Guazzelli[2]

[1)]*Univ. Bordeaux, CNRS, Syensqo, LOF, UMR 5258, F-33600 Pessac, France*

[2)]*Université Paris Cité, CNRS, Matière et Systèmes Complexes (MSC) UMR 7057, Paris, France*

(Dated: 18 March 2024)

Concentration inhomogeneities occur in many flows of non-Brownian suspensions. Their modeling requires describing the relative motion of the particle phase and of the fluid phase and accounting for their interaction, which is the object of the Suspension Balance Model (SBM). We systematically investigate the dynamics and the steady-state of shear-induced migration in a wide-gap Couette flow for a wide range of particle volume fraction, and we test the ability of the SBM to account for the observations. We use a model suspension for which macroscopic particle stresses are known. Surprisingly, the observed magnitude of migration is much lower than that predicted by the SBM when the particle stress in the model is matched with the macroscopic particle stress. Another remarkable observation is the quasi-absence of migration for semi-dilute suspensions. From the steady-state volume fraction profiles, we derive the local particle normal stress at the origin of shear-induced migration according to the SBM. However, the observed dynamics of migration is much faster than that predicted by the SBM when using this stress in the model. This suggests that there is a missing term in the usual macroscopic constitutive law for the particle normal stress driving migration. The SBM is indeed capable of accurately predicting both the magnitude and the dynamics of migration when a phenomenological term involving a concentration gradient is added to the particle normal stresses determined in macroscopic experiments.

I. INTRODUCTION

Suspensions of non-Brownian particles in a Newtonian fluid display non-Newtonian behaviors in the non-dilute regime, such as shear thinning, shear thickening, and normal-stress differences[1–3]. These behaviors have been found to be associated with the existence of direct interparticle frictional contacts. The often-observed shear thinning has been shown to result from non-Coulomb friction between the particles[4–7]. Shear thickening has been related to the emergence of frictional contacts when hydrodynamic forces overcome a short-range repulsive force between the particles[8–12]. Normal stress differences are known to stem from the anisotropic microstructure that forms due to direct contacts between pairs of rough particles, which break the fore-aft symmetry of purely hydrodynamic interactions[13,14].

From a micromechanical point of view, contacts impact the suspension total stress as the contribution to the bulk stress due to the presence of the particles contains both contact and hydrodynamic parts[1,15]. In the dense regime (typically for particle volume fraction $\phi \gtrsim 40\%$), the part coming from direct contact interactions between the particles even prevails over that coming from hydrodynamic interactions[16]. Knowledge of these stresses is essential to understand and model the non-Newtonian behaviors mentioned above. It is also key for understanding the concentration inhomogeneities that appear in many flows of non-Brownian suspensions and that are also a manifestation of non-Newtonian effects. While the bulk suspension is incompressible, the particle phase is compressible and can thus suffer density changes under the action of the normal components of the particle-phase stress. This later particle stress is a crucial element of the two-phase modeling of the suspension, termed the suspension balance model (SBM) in the case of viscous suspensions[17–20], which is detailed in Appendix A. It contains the same contact part as that included in the suspension total stress mentioned above, but also a hydrodynamic part that is more elusive, as it has been shown to differ from that contained in the suspension total stress[19,20].

Concentration inhomogeneities in suspensions are exemplified in the phenomenon of shear-induced migration of particles observed in Couette flows[21–24], tube and channel flows[25–27], and in extrusion geometries[28]. In such flows, the particles tend to migrate from the zones of high shear, where particle stresses are high, to the zones of low shear, where particle stresses are low. In other words, in these geometries, the particle normal stresses are unbalanced in the initially homogeneous suspension. This leads to particle migration, which stops when particle stress balance is achieved. This balance is ultimately reached owing to volume fraction inhomogeneities, since

particle stresses increase with increasing volume fraction. The SBM introduced above describes this migration phenomenon by relating the migration flux to the divergence of the normal stress of the particle phase; see Appendix A. Since there is a closure problem in the two-phase modeling, it is crucial to have robust constitutive rheological laws and, in particular, an accurate description of the particle stresses as a function of the shear rate and of the volume fraction.

Particle stresses are hard to measure experimentally. Specific rheometers have to be designed for their determination. They are all based on the same principle: the suspension is in contact with a grid of pore size smaller than the particle size, permitting the fluid to pass through but retaining the particles. In volume-imposed experiments, the fluid pressure is measured through the grid[29–31], and the particle stress normal to the grid is calculated as the total normal stress exerted on the same surface minus this fluid pressure. In pressure-imposed experiments, the particle pressure is directly applied onto the grid[32] and relative motion of the pure fluid and the grid leads to a change of the particle volume fraction until a steady state is reached; alternatively, the fluid can be sucked through the grid to impose the fluid pressure[33]. It is yet unclear whether the normal stresses measured in these experiments are identical to the particle normal stresses of the two-phase description of the SBM or not. They may account only for the contact contribution, as they are measured behind a grid and usually in the dense regime where contacts are dominant. It should also be noted that these measurements are performed in homogeneous suspensions, and therefore are unlikely to include the hydrodynamic part of the particle stresses involving concentration gradients (see Appendix A).

The overall macroscopic rheological description of the bulk and particle stresses that emerges for frictional suspensions of rigid spheres is given as follows. In a simple shear flow at a shear rate $\dot{\gamma}$, the suspension shear stress is

$$\tau = \eta_s(\phi/\phi_j)\eta_f\dot{\gamma}, \tag{1}$$

with η_f the suspending-fluid viscosity. The relative suspension viscosity η_s increases with increasing ϕ and diverges when approaching the jamming transition at the maximum flowable volume fraction ϕ_j. For frictional spheres, ϕ_j is smaller than the random close packing fraction and depends on the particle-size dispersion and on the frictional interactions between the particles[8]. In this framework, all non-linear effects are encoded in the possible dependence of ϕ_j on the applied shear stress[4,5,12,34]. For monodisperse frictional hard spheres, the dimensionless viscosity

$\eta_s(\phi/\phi_j)$ is well described by the Eilers function[3]

$$\eta_s(\phi/\phi_j) = \left(1 + \frac{5}{4}\frac{\phi}{1-\phi/\phi_j}\right)^2, \tag{2}$$

for a wide range of systems.

The particle normal stresses are less known. However, recent measurements tend to show that, defining the directions 1, 2, and 3, as the flow, the velocity gradient, and the vorticity directions, respectively, the particle normal stresses follow[3]:

$$\sigma_{11}^p \simeq \sigma_{22}^p \simeq 2\,\sigma_{33}^p, \tag{3}$$

$$\sigma_{22}^p = \eta_n(\phi/\phi_j)\eta_f\dot{\gamma}. \tag{4}$$

The exact values of the particle normal stress ratios are still debated[3]; moreover, these ratios may depend slightly on ϕ[30]. For the sake of simplicity, we use Eqs. (3) and (4) as it does not change significantly the conclusions of the present work.

The relative normal viscosity $\eta_n(\phi/\phi_j)$ has the same divergence as the relative shear viscosity at the approach of jamming. It can be rewritten as

$$\eta_n(\phi/\phi_j) = \frac{\eta_s(\phi/\phi_j)}{\mu(\phi/\phi_j)}, \tag{5}$$

where $\mu(\phi/\phi_j)$ is the macroscopic friction coefficient of the suspension. For frictional spheres, $\mu(\phi/\phi_j)$ is a decreasing function of ϕ/ϕ_j, which tends towards a finite value of order 0.3-0.4 at the jamming transition and diverges as ϕ vanishes.

Given the strong dependence of ϕ_j, and consequently of $\eta_s(\phi/\phi_j)$ and $\eta_n(\phi/\phi_j)$, on the details of interparticle interactions, it is crucial to obtain the complete information – suspension stresses, particle stresses, and volume fraction fields – on the same combination of fluid and particles if one wishes to achieve an in-depth testing of the SBM. As mentioned earlier, the non-linear macroscopic rheological behaviors in suspensions originate from microscopic particle-particle contact and interaction with the surrounding liquid. In particular, it has been shown that the same (polystyrene) particles dispersed in different solvents give rise to very different behaviors, linked to changes in the interparticle contact forces[7]. This is why it is important to study shear-induced migration for a reference mixture having a well-characterized rheological behavior.

Such consistent sets of data are unfortunately rare in the literature. E.g., in the seminal work of Morris and Boulay [18] on the SBM, data for the viscosity, normal stresses, and migration originate from different systems. The only consistent set of data that we are aware of is for PMMA

particles suspended in various mixtures of water and Triton X-100. For this combination, the macroscopic rheology (including particle stresses) has been characterized by Boyer, Guazzelli, and Pouliquen[32] with further confirmation by Etcheverry, Forterre, and Metzger[33], and shear-induced migration has been investigated in a pipe flow by Snook, Butler, and Guazzelli[27] and in Couette cells by Sarabian *et al.*[24] and d'Ambrosio, Blanc, and Lemaire[35]. The predictions of the SBM using the macroscopic rheological measurements of Boyer, Guazzelli, and Pouliquen[32] provide reasonable concentration profiles in the pipe flow experiments of Snook, Butler, and Guazzelli[27] at large bulk volume fraction, but discrepancies regarding the centerline concentration and the rate of migration are seen at bulk volume fractions $< 40\%$. The steady-state migration profiles found by d'Ambrosio, Blanc, and Lemaire[35] in a Couette cell are in good agreement with those predicted by the SBM with the particle stresses found by Boyer, Guazzelli, and Pouliquen[32]. However, d'Ambrosio, Blanc, and Lemaire[35] did not characterize the dynamics of migration. By investigating the transient and steady-state profiles in a Couette cell, Sarabian *et al.*[24] found that the particle stresses measured by Boyer, Guazzelli, and Pouliquen[32] actually fail to model the dynamics of migration when injected in the SBM. Discrepancies between the SBM and the experiments are also seen in the shear-induced resuspension experiments of d'Ambrosio, Blanc, and Lemaire[35,36] with negatively-buoyant suspension. In this case, no radial migration is observed, which seems inconsistent with the SBM and the particle stress determined in the same work.

In this paper, we propose to revisit this question by investigating in detail both the dynamics and the steady-state of shear-induced migration of a non-Brownian suspension in a wide-gap Couette geometry, in the whole range of bulk particle volume fraction. Our goal is to test the SBM and to see whether macroscopic particle stress measurements and migration data can be reconciled. We use a suspension which has been characterized extensively in the literature (more details are provided in Sec. II A and in Appendix B). Surprisingly, the observed magnitude of migration is much lower than that predicted by the SBM when the particle stress in the model is matched with the macroscopic particle stress. Another remarkable observation is the quasi absence of migration for semi-dilute suspensions. From the steady-state volume fraction profiles, we derive the local particle normal stress at the origin of shear-induced migration according to the SBM. However, the observed dynamics of migration is much faster than that predicted by the SBM when using this stress in the model. This suggests that there may be a missing term in the particle normal stress driving migration. The SBM is indeed capable of accurately predicting both the magnitude and the dynamics of migration when a phenomenological term involving a concentration gradient is

added to the particle normal stresses determined in macroscopic experiments.

In Sec. II, we describe the particles and fluid used in this study, and we recall the macroscopic results obtained for this system in the literature. We also present the setup used to measure velocity and concentration profiles, and show how the measurements can be analyzed to derive the suspension viscosity and the particle normal stress at the origin of migration. In Sec. III, we present the results regarding the steady-state and the dynamics of migration, and we compare the particle stress at the origin of migration according to the SBM to that measured in macroscopic experiments. In Sec. IV, we finally compare the predictions of the SBM to the experimental observations for three different sets of constitutive equations. Conclusions are drawn in Sec. V.

II. EXPERIMENTAL TECHNIQUES

A. Particles and fluid

We study suspensions of monodisperse spherical particles in a Newtonian fluid. The particles are polystyrene (PS, from MicroBeads) beads of density 1.05 and of 140 μm diameter, with a 5% dispersion in size. The fluid is poly(ethylene glycol-ran-polypropylene glycol) monobutyl ether (PEG, from Sigma); its viscosity is $\eta_f = 2.1$ Pa.s at 25°C and its density is 1.05. There is negligible density difference between the particles and the fluid, which is supported by vertical volume fraction profiles measurements, which show no sign of sedimentation or creaming during the experiments. Suspensions have been prepared at various volume fractions ranging from the semi-dilute to the dense regime: 6%, 10%, 14%, 18%, 20%, 23%, 26%, 30%, 40%, 45%, 50%, 53%, 54.5%, and 56%.

An advantage of suspensions of PS beads suspended in PEG is that their macroscopic behavior has been documented by several groups in the literature. The same system as that presently used has been studied by Deboeuf *et al.* [29] and Garland *et al.* [31], who have measured the shear stress τ and the interstitial fluid pressure p^f in a Couette geometry; in addition, Garland *et al.* [31] have measured the normal stress σ_{22}, which, in combination with p^f, provides the particle stress σ_{22}^p. This system has also been studied by Boyer, Pouliquen, and Guazzelli [37], who have characterized the shear viscosity of homogeneous suspensions. Other data have been obtained by Boyer, Guazzelli, and Pouliquen [32] and Tapia, Pouliquen, and Guazzelli [34] on larger PS particles (of 580 μm diameter) in PEG, with a pressure-imposed rheometer; they have obtained the particle stress σ_{22}^p and

the suspension shear stress τ in the dense regime, i.e., for $\phi \gtrsim 45\%$. Other relevant data have been obtained with the same PS particles (of 140 μm diameter) suspended in a fluid of very close physicochemical nature – a polyalkylene glycol (UCON oil 75H90000 from Dow) mixed with a water solution – by Dbouk, Lobry, and Lemaire [30], who have characterized both the macroscopic behavior and the particle stresses within a parallel-plate geometry thanks to a combination of interstitial-fluid pressure and normal stress profiles measurements. All these data are shown and discussed in Appendix. B, and compared with our local data in Sec. III A.

B. Methods

We study the flows of the suspensions in a wide-gap Couette geometry with the help of Nuclear Magnetic Resonance (NMR) techniques, which provide the suspension velocity and particle volume fraction profiles as a function of time. This setup has been described in detail several times elsewhere[23,38,39]. We give here a short description and discuss how the data can be processed to extract a shear viscosity and a particle normal stress.

We use a wide-gap Couette geometry of inner radius $R_\mathrm{i} = 3$ cm and outer radius $R_\mathrm{o} = 5.1$ cm. The inner cylinder height is $H = 11$ cm; it is inserted at 2 cm from the bottom of the cup to avoid end-effects affecting the flow within the gap[40]. We use a serrated cylinder (roughness, 500 μm) to avoid wall slip[41]. We did not observe any velocity discontinuity close to the cylinders, which is consistent with a negligible wall slip. The Couette cell is inserted in a Magnetic Resonance Imaging (MRI) scanner and proton NMR[42,43] is used as a non-intrusive technique to measure the local material velocity and the local particle concentration inside the gap. Experiments are performed with a 0.5 T proton MRI scanner (Bruker Advance 24/80 DBX) operating at 20 MHz. It is equipped with a birdcage RF coil (20 cm inner diameter) and a 3D gradient system (BGA26-Bruker). We use a home-made NMR-compliant rheometer fully described in Ref. 38.

All data are averaged over 2 cm in the middle of the cell in the vertical direction, over 1 cm in the azimuthal direction, and measured with a resolution of 110 μm in the radial direction. We checked the homogeneity of the velocity and concentration profiles along the vertical direction, which justifies averaging data. Note that in the sequences we use, only NMR signal originating from the hydrogen nuclei belonging to the liquid phase of the sample is recorded.

Azimuthal velocity profiles $V(r)$ are obtained with a combination of a spin-echo–spin-warp imaging technique and a phase-encoded velocimetry[42,43]; more details are found in Refs. 38, 44,

and 45. A single velocity measurement may take as little as 1 s. Particle concentration profiles $\phi(r)$ are obtained with a spin-echo sequence[42]; NMR data are recorded during a readout gradient and Fourier transformed in order to obtain information about the hydrogen density in the liquid phase along the radial direction; more details can be found in Ref. 23. A concentration profile is evaluated in 3 min. It can be measured either on the material at rest after a given shear history or on the flowing material when the rotational speed is lower than 20 rpm (otherwise the signal is lost during the measurement). In order to characterize the dynamics of shear-induced migration, we have chosen here to rely on the velocity profiles evolution in time, which have a much better accuracy than the concentration profiles and can be measured continuously in time.

In the experiments, we control the rotational speed Ω of the Couette cell inner cylinder. The setup is not equipped with a torque probe. To measure the torque, the same experiment has to be performed again with a rheometer in order to obtain the torque $T(\Omega)$ relationship, as done in Ref. 23. As we show below, this is not a necessary step to analyze the results.

For each experiment, after loading the material, we first measure the volume fraction profile at rest in order to check that the material is initially homogeneous. We have observed that all suspensions prepared at volume fraction ϕ ranging from 6 to 54.5% are initially homogeneous; an example is shown in Appendix C. The most concentrated suspension that we have prepared ($\phi =$ 56%) is initially inhomogeneous due to the shear flow induced by the loading (see Appendix D); we did not study this suspension further.

Afterward, we apply a constant rotational speed Ω ranging from 1 to 120 rpm, and we measure continuously the evolution of the suspension velocity $V(r,t)$ in time until steady-state is reached. For viscous suspensions, it is more relevant to study the dynamics as a function of strain than as a function of time; this is confirmed in our experiments, where changing the rotational speed by two orders of magnitude leads to the same velocity variations as a function of strain. Here, we simply estimate the macroscopic strain Γ as

$$\Gamma = \Omega t. \tag{6}$$

When steady-state is reached, we stop the rotor rotation, and we measure the volume fraction profile $\phi(r)$ on the fully migrated state. NMR does not provide quantitative concentration measurements near the edges[23]. Therefore, the volume fraction cannot be accessed in a 2–3-mm zone near the inner and outer cylinders. However, the velocity can be measured in these zones.

From these measurements, we extract the local suspension viscosity and the local friction coefficient as a function of the local particle volume fraction using the procedure described below.

Local viscosity measurement

The local shear rate $\dot{\gamma}(r)$ at a radial position r in the gap can be deduced from $V(r)$ as

$$\dot{\gamma}(r) = V(r)/r - \partial_r V(r). \tag{7}$$

The derivative $\partial_x f$ with respect to coordinate x of experimental data $f(x_i)$ measured at regularly spaced positions x_i is here computed as $\partial_x f(x_i) = [f(x_{i+1}) - f(x_{i-1})]/[x_{i+1} - x_{i-1}]$. The stress distribution $\tau(r)$ within the gap is obtained from the stress balance equation, which yields

$$\tau(r) = \frac{T(\Omega)}{2\pi r^2 H}, \tag{8}$$

when the material is homogeneous along the vertical direction.

When a steady-state volume fraction profile $\phi(r)$ is reached, a change of variables can be performed between r and ϕ in the above equations. A local stress/strain-rate relationship $\tau(\dot{\gamma}, \phi)$ at a fixed and well-defined volume fraction $\phi(r)$ is then obtained by collecting the measurements of local stress $\tau(r)$ and shear rate $\dot{\gamma}(r)$ for this single fixed r. The suspension viscosity as a function of volume fraction follows as

$$\eta(\phi(r)) = \frac{\tau(r)}{\dot{\gamma}(r)}. \tag{9}$$

By collecting data in the whole gap within the inhomogeneous suspension, a portion of the viscosity volume fraction relationship $\eta(\phi)$ is finally obtained for $\phi(R_\mathrm{i}) < \phi < \phi(R_\mathrm{o})$. More details on this methodology and its application can be found in Refs. 23, 46, and 47.

In principle, torque measurements $T(\Omega)$ need to be performed. However, it can be noted that the relative variation of the viscosity within the gap, as compared to a reference position R_1 in the gap where the volume fraction is $\phi(R_1)$, is quantitatively estimated as

$$\frac{\eta(\phi(r))}{\eta(\phi(R_1))} = \frac{R_1^2}{r^2}\frac{\dot{\gamma}(r)}{\dot{\gamma}(R_1)}, \tag{10}$$

which does not require any torque measurement. The relative variation of the viscosity η with the volume fraction ϕ over the whole range of ϕ can finally be inferred by combining local data measured at various average volume fraction. We build this curve by continuity, i.e., by overlapping data obtained at a same local ϕ value for different average volume fractions. To obtain a quantitative $\eta_\mathrm{s}(\phi)$ curve, a last step is necessary. It consists in matching the local viscosity measured at a given local ϕ value with that measured in a macroscopic experiment on a homogeneous suspension at the same ϕ value. Here, we have chosen to match the local data with the macroscopic data

obtained at a moderate $\phi = 30\%$ in order to infer the whole local $\eta_s(\phi)$ curve; at this value of ϕ, significant viscosity variation can indeed be measured macroscopically without being flawed by migration. As shown in Sec. III, we did not obtain data in the range between 32% and 36%; local data have thus been extrapolated in this range to ensure continuity of the local curve.

Local particle stress measurement

From the SBM discussed in Appendix A, *in the absence of a diffusion term of hydrodynamic origin in the migration equation* (A10), the steady state volume fraction profile $\phi(r)$ is such that

$$\frac{\eta_n(\phi(r))}{\eta_s(\phi(r))} = \frac{1}{\mu(\phi(r))} = A\, r^2, \tag{11}$$

where the phenomenological expression (3) introduced in Sec. I is used, and the proportionality factor A is obtained by ensuring mass conservation. To obtain the friction coefficient $\mu(\phi)$ from the experiments, as for the local $\eta_s(\phi)$ curve, we have chosen to build this curve step by step. Assuming that the value of $\mu(\phi)$ is known at a given position R_1 in the gap, where the volume fraction is $\phi(R_1)$, a portion of the $\mu(\phi)$ curve, for $\phi(R_i) < \phi < \phi(R_o)$, can be inferred from

$$\mu(\phi(r)) = \mu(\phi(R_1))\frac{R_1^2}{r^2}. \tag{12}$$

Then, by combining local data obtained at various average volume fraction, the relative variation of the friction coefficient $\mu(\phi)$ with the volume fraction ϕ over the whole range of ϕ can be obtained. A quantitative $\mu(\phi)$ curve is finally achieved by matching the local friction coefficient measured at a given local ϕ value with that measured in a macroscopic experiment on a homogeneous suspension at the same ϕ value. Here, we have chosen to match the local data with the expected behavior at jamming by extrapolating our data at the jamming volume fraction. Experimental and numerical data from the literature[8,32,33] have indeed found that $\mu \simeq 0.35$ close to jamming for frictional suspensions, and that this value is rather insensitive to small variations in the particle properties[8]. As for the local viscosity, we did not obtain data in the range between 32% and 36%; local data have thus been extrapolated in this range to ensure continuity of the local curve. We emphasize that this determination of a local $\mu(\phi)$ is valid only under the assumption that $D_{12} = 0$ in Eq. (A10) which is the common assumption found in the literature.

III. EXPERIMENTAL RESULTS AND COMPARISON WITH THE SBM PREDICTIONS

A step by step analysis of the case of a 40% suspension is presented in Appendix C, to show in detail how the data are processed. In this section, we present the data resulting from the same analysis performed on all the studied suspensions.

In Sec. III A, we start by showing the steady-state velocity and volume fraction profiles. We then extract the $\eta_s(\phi)$ and $\mu(\phi)$ relationships from these measurements, as detailed in Sec. II B. These data are compared to data from the literature presented in Sec. II A and shown in Appendix B. In Sec. III B, we then show how shear-induced migration occurs by studying the velocity profiles evolution in time. The predictions of the SBM (presented in Appendix A) will be compared to the experimental results and discussed in Sec. IV.

A. Steady state

1. Velocity and volume-fraction profiles

For clarity, only half of the measured steady-state profiles are gathered in Fig. 1, in the form of local volume fraction variations and of dimensionless velocity profiles. Other profiles are shown in Sec. IV. We recall that quantitative volume fraction measurements cannot be performed in a 2-3 mm region near the walls, which explains the lack of data in these regions.

In Fig. 1a, we first note that, within the experimental absolute uncertainty, previously estimated to be $\pm 0.2\%$[23], the 6% suspension remains homogeneous, even after a very long time of shear corresponding to a total macroscopic strain $\Gamma = 7.5\,10^5$. Shear-induced migration from the inner cylinder to the outer cylinder is observed for all other studied volume fractions. The amplitude of the volume fraction variations increases regularly as the average volume fraction is increased. The absolute variation is of order 1% from the inner cylinder to the outer cylinder for a 10% suspension, of order 5% for a 40% suspension, and of order 7% for a 54.5% suspension (Fig. 1a). The relative volume fraction variation thus seems to be of the same order of magnitude for all suspensions, and is of order 10 to 15%. The ϕ variations may thus be too small to be experimentally measurable in the 6% suspension, although it is possible that there is no migration at small $\phi \lesssim 6\%$, .

Consistently, the steady-state velocity profile of the 6% suspension is well-fitted to the profile of a homogeneous Newtonian fluid (Fig. 1b). As the volume fraction is increased, the velocity pro-

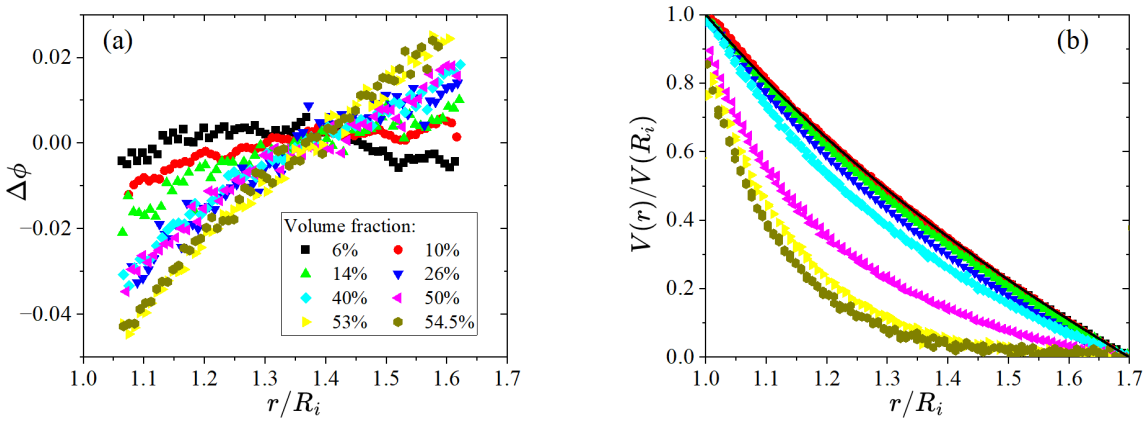

FIG. 1. (a) Local volume fraction variations $\Delta\phi(r)$ (average volume fraction subtracted from the steady-state volume fraction profiles) and (b) steady state dimensionless velocity profiles $V(r)/V(R_\mathrm{i})$, for suspensions of 6%, 10%, 14%, 26%, 40%, 50%, 53%, and 54.5% average volume fraction (see legend). The data are plotted as a function of the dimensionless radial position r/R_i. The full line in (b) is the theoretical velocity profile for a homogeneous Newtonian fluid.

files become more curved: the velocity decreases more and more rapidly with the radial position near the inner cylinder. This is consistent with the shear-induced migration observed in Fig. 1a. Indeed, the shear stress variation within the gap, from the inner cylinder to the outer cylinder, is $R_\mathrm{i}^2/R_\mathrm{o}^2$ in all cases (Eq. (8)). The resulting shear rate variation, which dictates the velocity curvature, is then $\left(\eta_\mathrm{s}(\phi(R_\mathrm{i}))/\eta_\mathrm{s}(\phi(R_\mathrm{o}))\right)\left(R_\mathrm{i}^2/R_\mathrm{o}^2\right)$. This ratio becomes larger as the average volume fraction increases for two reasons: (i) $\phi(R_\mathrm{i})-\phi(R_\mathrm{o})$ increases and (ii) the viscosity variations increase (in other words, the second derivative of the viscosity is positive for all ϕ).

2. *Local rheology*

By combining the information given by the velocity profiles and the concentration profiles, as detailed in Sec. II B, we build the local dimensionless viscosity and friction coefficient curves as a function of volume fraction in Fig. 2.

The local viscosity data are in good agreement with the macroscopic data up to a 45% volume fraction. At higher volume fraction, the local data are lower than the macroscopic data, and, consequently, the data are not perfectly fitted to the rheological law – Eq. (B1) – of Boyer, Guazzelli, and Pouliquen[32], which nevertheless provides a reasonable correlation.

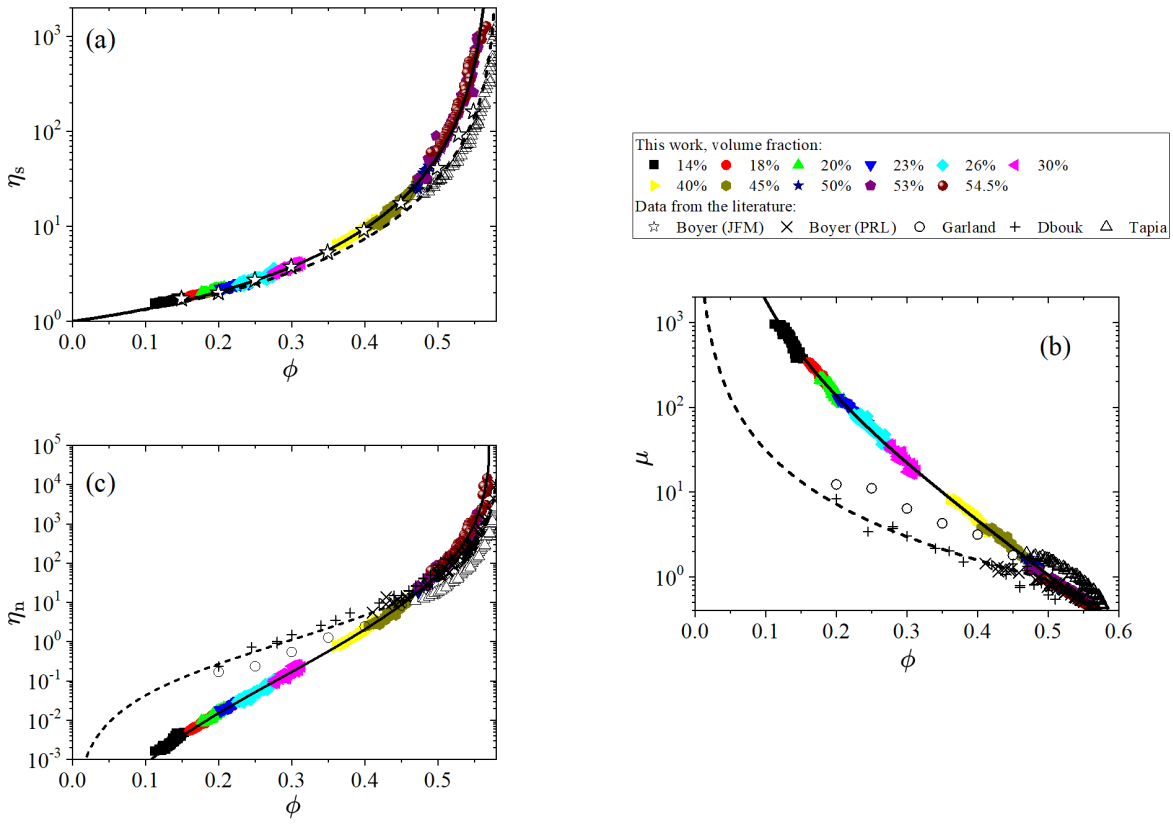

FIG. 2. (a) Local dimensionless viscosity η_s, (b) local friction coefficient μ, and (c) local normal viscosity η_n as a function of the local volume fraction ϕ, from experiments performed at various average volume fraction (see legend). Macroscopic measurements from the literature by Dbouk, Lobry, and Lemaire [30], Garland *et al.* [31], Boyer, Guazzelli, and Pouliquen [32], Tapia, Pouliquen, and Guazzelli [34], Boyer, Pouliquen, and Guazzelli [37] are also shown (see legend). For clarity, only the data of Boyer, Pouliquen, and Guazzelli [37] and Tapia, Pouliquen, and Guazzelli [34] are shown in (a). We recall that the local η_n and μ are deduced from the steady-state volume fraction profiles under the assumption that there is no additional diffusion term in the SBM. The dashed lines are the rheological laws – Eqs. (B1), (B2) and (B3) – of Boyer, Guazzelli, and Pouliquen [32]. The full lines are the phenomenological laws Eqs. (13), (14) and (15).

Here, we find that the data are very well fitted to the simple viscosity function

$$\eta_s(\phi) = 1 + (5/2)\phi(1-\phi/\phi_j)^{-1} + (\phi/\phi_j)^2(1-\phi/\phi_j)^{-2}, \tag{13}$$

with $\phi_j = 0.575$. Note that this equation is simply Eq. (B1) with $\mu^c(\phi) = 1$. It has the advantage of matching the $(\phi_j - \phi)^{-2}$ divergence near jamming with the Einstein limit at low ϕ.

The discrepancy between local and macroscopic measurements at the approach of jamming

may have two possible origins. First, ϕ_j is very sensitive to any variation of the interparticle friction coefficient. Although we used the same PS particles as Boyer, Guazzelli, and Pouliquen [32] and Tapia, Pouliquen, and Guazzelli [34] in the same fluid, the particles have a different diameter, and may thus have slightly different frictional properties. Another possibility is shear-induced migration affecting the macroscopic measurements, although migration is expected to be limited when using annular parallel plate[18] as in the experiments of Tapia, Pouliquen, and Guazzelli [34]. Due to the viscosity divergence when approaching ϕ_j, macroscopic measurements performed in dense suspensions are affected by any subtle change in the material volume fraction[23], and migration is very hard to avoid as its development gets faster when the volume fraction is increased; it can even occur during the material loading as shown in Appendix D for a 56% suspension.

The friction coefficient data obtained from local measurements are very different from those obtained in macroscopic measurements, except in the dense regime. Close to jamming, the data have been built to match the macroscopic measurements (Sec. II B). Then, as ϕ is decreased, the local $\mu(\phi)$ follows the same evolution as that observed by Boyer, Guazzelli, and Pouliquen [32] down to a 50% volume fraction. It subsequently increases much more than the macroscopic data. When ϕ is decreased from 56% to 20%, the macroscopic friction coefficient typically increases by a factor 10, whereas the local $\mu(\phi)$ increases by a factor 100. This discrepancy is not expected to be due to an artefact of the macroscopic measurements. It may be due to the fact that the particle stress measured in macroscopic experiments only accounts for direct interparticle contacts and thus is missing terms of hydrodynamic origin, as noted in Sec. I and developed in Sec. A. In dense suspensions, however, contact forces are dominant and the impact of hydrodynamic forces is negligible[3], which might explain the good match above 50%. We will discuss this point further when modeling migration with the SBM in Sec. IV.

To find a correlation for $\mu(\phi)$ that can be used in the SBM, we need an expression that is consistent with a strong divergence ($\sim \phi^{-3}$) at low ϕ and with Eq. (B2) for ϕ close to ϕ_j. We propose the following ad-hoc expansion in $(\phi_j/\phi)(1-\phi/\phi_j)$:

$$\mu(\phi) = \mu_0 + \alpha_1 * \Big(\frac{\phi_j}{\phi}(1-\frac{\phi}{\phi_j})\Big) + \alpha_2\Big(\frac{\phi_j}{\phi}(1-\frac{\phi}{\phi_j})\Big)^2 + \alpha_3\Big(\frac{\phi_j}{\phi}(1-\frac{\phi}{\phi_j})\Big)^3, \tag{14}$$

with $\mu_0 = 0.35$, $\alpha_1 = 3$, $\alpha_2 = 9$, and $\alpha_3 = 15$, which provides a good fit to our experimental data (together with $\phi_j = 0.575$, as found for the viscosity). At this stage, this correlation should only be considered as a convenient way of modeling the data in order to test the SBM.

From the local dimensionless viscosity $\eta_s(\phi)$ and the local friction coefficient $\mu(\phi)$, the local

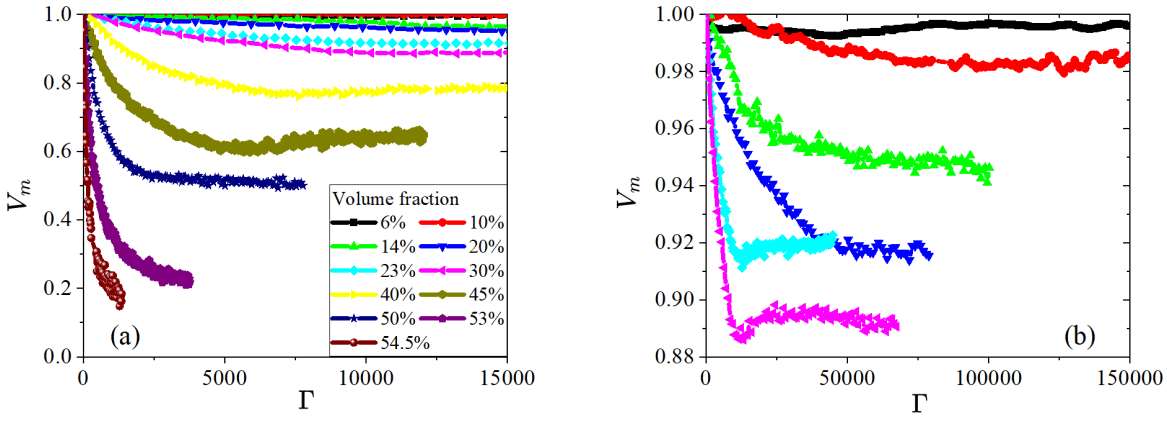

FIG. 3. Evolution of the dimensionless velocity V_m measured in the middle of the gap as a function of the macroscopic strain $\Gamma = \Omega t$, for suspensions of different average volume fraction (see legend). (a) and (b) present the same data with different scales for the two axes in order to highlight the fast migration occurring at high ϕ (a) and the slow migration occurring at low ϕ (b).

normal viscosity $\eta_n(\phi)$ can be computed as $\eta_n(\phi) = \eta_s(\phi)/\mu(\phi)$. The local $\eta_n(\phi)$ data are plotted in Fig. 2c, together with macroscopic measurements from the literature. Local and macroscopic data show some difference in the whole range of volume fraction. The local data are very well fitted to the function obtained by combining Eqs. (13) and (14):

$$\eta_n(\phi) = \frac{\eta_s(\phi)}{\mu(\phi)} = \frac{1 + (5/2)\phi(1-\phi/\phi_j)^{-1} + (\phi/\phi_j)^2(1-\phi/\phi_j)^{-2}}{\mu_0 + \alpha_1 * \left(\frac{\phi_j}{\phi}(1-\frac{\phi}{\phi_j})\right) + \alpha_2\left(\frac{\phi_j}{\phi}(1-\frac{\phi}{\phi_j})\right)^2 + \alpha_3\left(\frac{\phi_j}{\phi}(1-\frac{\phi}{\phi_j})\right)^3}, \qquad (15)$$

with $\phi_j = 0.575$, $\mu_0 = 0.35$, $\alpha_1 = 3$, $\alpha_2 = 9$, and $\alpha_3 = 15$.

B. Dynamics

In order to study the dynamics of shear induced migration, as discussed in Appendix C, it is convenient to plot the time evolution of the suspension velocity in the middle of the gap of the Couette geometry, which is very sensitive to the progressive establishment of volume fraction gradients. The data are shown in Fig. 3 for all the studied suspensions. As observed on the steady-state velocity profiles, the amplitude of the velocity variation increases with increasing volume fraction. Moreover, the dynamics of this variation becomes faster.

To quantify the impact of volume fraction on the dynamics of migration, we plot in Fig. 4 the strain $\Gamma_{1/2}(\phi) = \Omega * t_{1/2}(\phi)$ at which half of the velocity variation is observed. This strain $\Gamma_{1/2}$

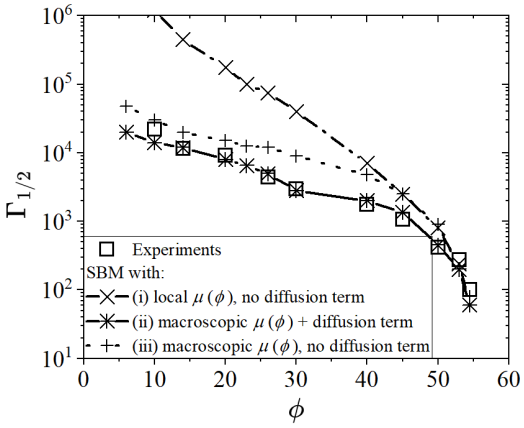

FIG. 4. Macroscopic strain $\Gamma_{1/2}(\phi) = \Omega * t_{1/2}(\phi)$ at which half of the velocity variation is observed in the middle of the gap vs. average volume fraction ϕ: experimental data (empty squares) and prediction of the SBM in the three cases described in the text (see legend).

decreases from $\simeq 20000$ to $\simeq 100$ when ϕ increases from 10% to 54.5%. The decrease of $\Gamma_{1/2}$ with ϕ becomes faster when approaching jamming, with a decrease by a factor 10 from $\phi = 45\%$ to $\phi = 54.5\%$.

IV. COMPARISON WITH THE SBM

In this section, we test the predictions of the SBM against the present experiments. As detailed in Appendix A, migration is driven by the divergence of the normal stress of the particle phase. However, macroscopic measurements of this normal stress may only include its contact portion; besides, they are performed on uniform suspensions. We have thus tentatively added a phenomenological term involving a concentration gradient as suggested by Lhuillier [19], i.e., a possible diffusion term (characterized by a diffusion coefficient D_{12}, see Eq. (A10)). To be comprehensive, we propose to test three different constitutive laws:

(i) We first consider the rheological laws given by Eqs. (13) and (14). These equations come from the local rheology data derived from the steady-state velocity and volume fraction profiles under the usual assumption $D_{12} = 0$ in the SBM (Eq. (A10)). With these constitutive equations, the dynamics of the SBM is thus solved for $D_{12} = 0$ only.

(ii) Since the particle stress, as measured in macroscopic experiments, likely accounts for direct

interparticle contacts only and is not consistent with Eq. (14), we also solve the SBM with Eq. (B3) for $\mu(\phi)$ and Eq. (13) for $\eta_s(\phi)$, together with $D_{12} \neq 0$ in Eq. (A10) to account for a possible term of hydrodynamic origin in the stress driving migration. Eq. (B3) is indeed in very good agreement with direct measurements of the particle stresses for our suspension in the literature (see Appendix B, Fig. 7). Eq. (13) is used for $\eta_s(\phi)$ as it is consistent with the local viscosity measurements, in order to make sure that the velocity profiles are correctly accounted for by the model. $D_{12}(\phi)$ is set as a free parameter, which *a priori* depends on ϕ.

(iii) The same model is used as in (ii), but with the usual assumption $D_{12} = 0$ in the SBM for the sake of comparison, and to understand better the impact of introducing a nonzero diffusion coefficient in (ii).

1. Steady-state

Comparison of the steady state profiles inferred from the experiments and from the predictions of the SBM using the three rheological laws described above are shown in Fig. 5 for nine of the studied suspensions.

Case (i). Of course, since Eqs. (13) and (14) have been built from the steady-state velocity and concentration profiles by assuming $D_{12} = 0$ in the SBM, a good agreement with the experimental data is obtained when they are used in the SBM to compute the theoretical steady-state profiles. The crucial test of the SBM lies here in the prediction of the dynamics of migration, which is studied in the next section. It remains interesting at this stage to discuss the prediction for semi-dilute suspensions, as it was not possible to derive local $\mu(\phi)$ data from the profiles for $\phi \lesssim 10\%$. Very limited migration is predicted for the 10% suspension, with a variation from 8.5% close to the inner cylinder to 11% close to the outer cylinder, which is in fair agreement with the observed volume fraction profile. For the 6% suspension, the volume fraction is predicted to vary only from 5% close to the inner cylinder to 6.8% close to the outer cylinder; this is possibly too small for the sensitivity of the NMR technique; it might also be that the divergence of $\mu(\phi)$ at low ϕ is even more abrupt than that extrapolated from the data in Eq. (14).

Case (iii). When $D_{12} = 0$ is assumed in the SBM, and $\mu(\phi)$ is modeled by Eq. (B3), consistent with the macroscopic measurements, the SBM predicts migration with a much larger magnitude than that observed experimentally for all volume fractions below 50%, consistent with the observed discrepancy between the local and macroscopic $\mu(\phi)$ data. In the specific case of

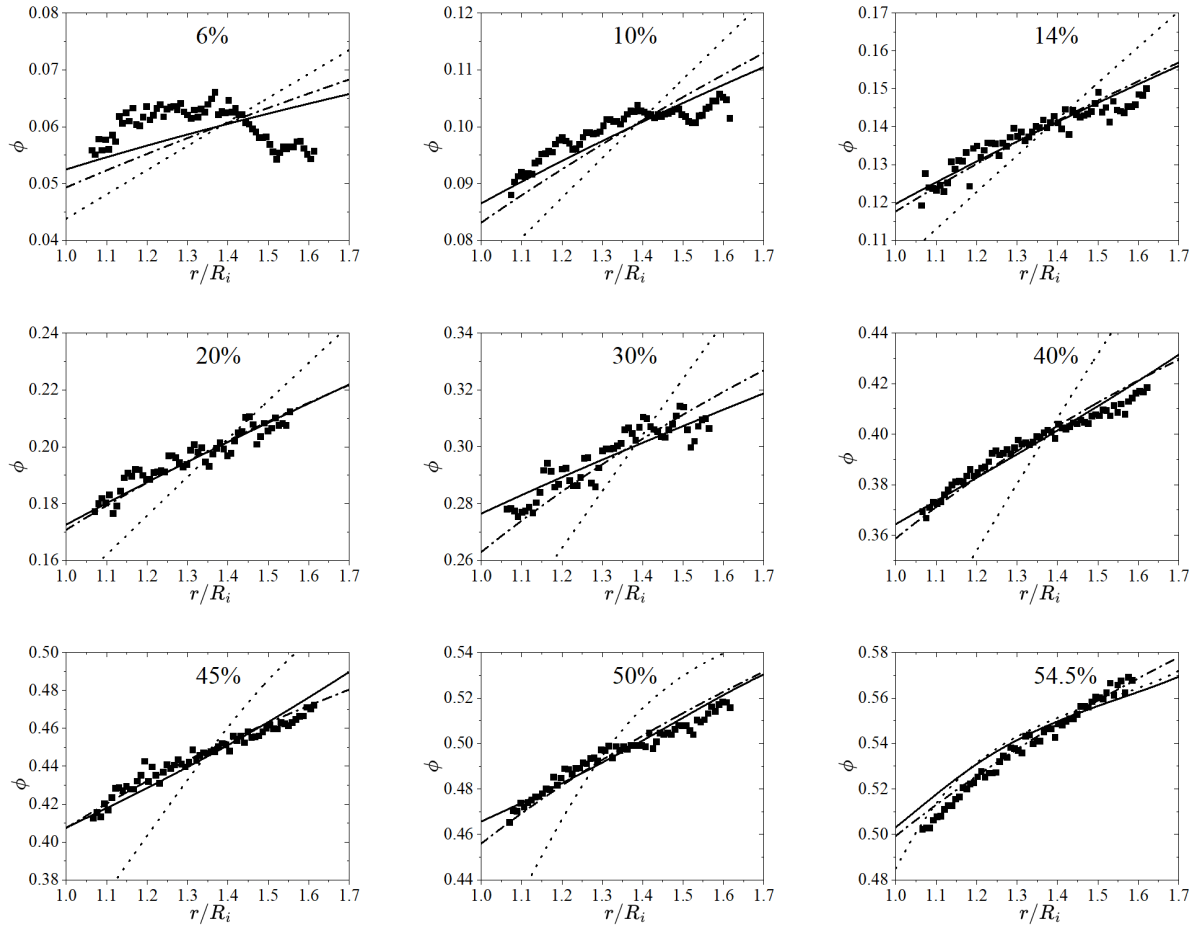

FIG. 5. Steady state volume fraction profiles: experimental data (squares) and predictions of the SBM (lines) with the three sets of equations described in the text [(i): dashed-dotted line, (ii): solid line, and (iii): dotted line]. The average volume fraction of the studied suspension is, from left to right and from top to bottom: 6%, 10%, 14%, 20%, 30%, 40%, 45%, 50%, 54.5%.

the 6% volume fraction, the model predicts measurable shear-induced migration, in contrast with our observation. In the dense regime, the predictions are in fair agreement with the experiments, consistent with the good match between the macroscopic and local data for $\phi > 50\%$.

Case (ii). When $D_{12}(\phi)$ is added as a free ϕ-dependent parameter, with values reported in Tab. I, the SBM predictions match all the experimental volume fraction profiles, as the diffusive term limits the magnitude of migration as compared to that expected from the sole contact contribution. The crucial test of this rheological model now lies in the comparison between the predicted and observed dynamics, discussed in the next section.

ϕ	6%	10%	14%	20%	23%	26%	30%	40%	45%	50%	53%	54.5%
D_{12}	10	10	10	15	20	30	75	150	250	1000	500	1000

TABLE I. Diffusion coefficient D_{12} used to model both the steady-state data and the dynamics of migration in case (ii), for all average volume fractions ϕ investigated.

2. Dynamics

The predictions of the dynamics of migration for nine of the studied suspensions in the three cases described above are shown in Fig. 6, where the evolution of the velocity V_m in the middle of the gap of the Couette geometry is plotted as a function of the macroscopic strain Γ. To summarize the predictions of three cases investigated, we also plot in Fig. 4 the strain $\Gamma_{1/2}(\phi)$ at which half of the velocity variation is found.

Case (i). Although the steady-state profiles are very well described by the SBM in this case, the predicted dynamics of migration is much slower than that observed experimentally when $\phi \lesssim 45\%$. As clearly observed in Fig. 4, the departure from the experimental data increases with decreasing ϕ. This shows that the proposed rheological model fails in describing the migration flux. Interestingly, there is a fair agreement between the predictions and the observations for dense suspensions with $\phi \gtrsim 50\%$. This may suggest that contacts provide the dominant contribution to migration and that there is no need to account for any additional hydrodynamic contribution in this dense regime.

Case (iii). When $D_{12} = 0$ is assumed in the SBM, and $\mu(\phi)$ is modeled by Eq. (B3), the predicted dynamics of migration is systematically slower than that observed experimentally. Interestingly, the relative variation of $\Gamma_{1/2}(\phi)$ with ϕ shows nonetheless the same trend as the experimental observation. Close to jamming, at $\phi = 54.5\%$, the predictions are in good agreement with the experiments, which is consistent with the good match between the macroscopic and local data for $\phi > 50\%$ in Fig. 2.

Case (ii). When $D_{12}(\phi)$ is given by the values of Tab. I which give a good match between the predicted and the observed steady-state profiles, a remarkable agreement between the predicted and the observed dynamics is observed as well, in the whole range of investigated volume fractions. As compared to the case $D_{12} = 0$, the introduction of a diffusion coefficient simultaneously decreases the magnitude of migration and accelerates its dynamics, in quantitative agreement with

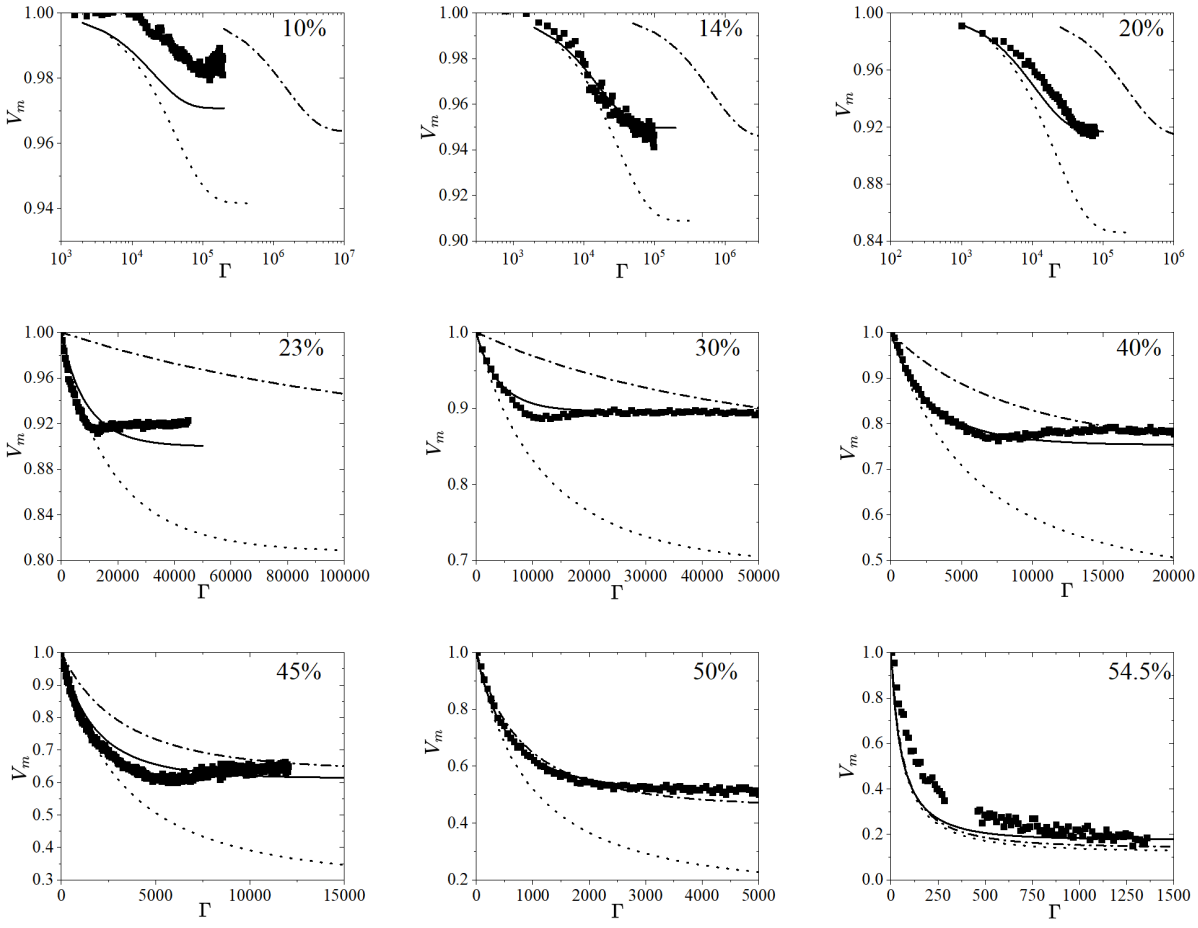

FIG. 6. Evolution of the velocity V_m in the middle of the gap as a function of the macroscopic strain $\Gamma = \Omega t$: experimental data (squares) and predictions of the SBM (lines) with the three sets of equations described in the text [(i): dashed-dotted line, (ii): solid line, and (iii): dotted line]. The average volume fraction of the studied suspension is, from left to right and from top to bottom: 10%, 14%, 20%, 23%, 30%, 40%, 45%, 50%, 54.5%. A semi-log scale is used for clarity for $\phi \lesssim 20\%$.

the observations in both cases.

V. DISCUSSION AND CONCLUSIONS

In this work, we have investigated shear-induced migration for a model suspension for which macroscopic measurements of the bulk and particle stresses can be found in the literature. We have provided crucial testing of the SBM by comparing its predictions against both the dynamics and the steady-state of shear-induced migration in a wide-gap Couette device.

The SBM describes shear-induced migration by relating the migration flux to the divergence of the normal stress of the particle phase. This modeling thus relies on having a robust macroscopic description of the particle stress. Most of the macroscopic measurements of this particle stress, however, may only account for the contact contribution, which prevails at large concentrations, and may miss the hydrodynamic contribution, which is likely to be of importance for moderate concentrations. Another problem is that these measurements are performed on uniform suspensions and may thus fail to capture forces acting on the particles and involving their concentration gradient or the gradient of the shear rate[19].

If we use the simplest form of the SBM (without any diffusive gradient term), although a particle stress consistent with the steady-state profiles can be derived, it is not possible to match the SBM prediction with the observed dynamics as migration happens to be much faster than predicted. However, when the particle stress in the model is matched with the particle normal stress determined in macroscopic experiments, and when a tentative diffusive gradient term is added to the SBM, both the magnitude of migration and its dynamics are correctly accounted for.

The main output of this work is to evidence this missing term in the usual macroscopic constitutive law for the particle normal stress driving migration. At large concentrations, this term is not so crucial as good agreement is obtained when dropped. This is consistent with the prevalence of contacts at large concentrations. It is however crucial at moderate concentrations, where hydrodynamic interactions become important. Another remarkable observation is the quasi absence of migration for semi-dilute suspensions, which is accounted for by the model with a diffusion term.

It would now be interesting to test how adding such a phenomenological diffusive term impacts the predictions of the SBM for other flow geometries. For a Poiseuille flow, these predictions can be easily computed. Using the same parameters as those found in the present paper, we show in Appendix E that it might reconcile the SBM predictions and the experimental results. Indeed, adding a diffusive gradient to the SBM, with the same D_{12} values as in our experiments in the Couette cell, provides a better agreement with the experiments of Snook, Butler, and Guazzelli[27] than when the standard SBM, with $D_{12} = 0$, is considered. The case of shear-induced resuspension is more complex to analyze as the fluid mechanics problem is 2D. It would deserve a thorough analysis with the help of simulations in a Couette cell. We hypothesize that, in this problem, shear-induced migration in the radial direction might be inhibited due to a diffusion term $\sim \eta_f \dot{\gamma} \phi D_{23} \frac{\partial \phi}{\partial z}$ related to the vertical concentration gradient (see Eq. A7), which would explain the absence of radial migration in the experiments of d'Ambrosio, Blanc, and Lemaire[35].

Appendix A: Suspension balance model (SBM)

The Suspension Balance Model (SBM) has been developed to model macroscopic spatial variation of the particle volume fraction ϕ due to particle migration in dispersions of rigid neutrally buoyant particles submitted to shearing flows at low Reynolds number[17–20]. The equations of motion are deduced from a two-phase approach of the particulate system in which the particles and the fluid are considered as interpenetrating continua. There is a large literature around the ways of averaging the balances of mass and momentum at any point of the suspension[48,49]. The resulting averaged equations can be written by considering either the two phases (fluid and particles) or one phase (fluid or particles) and the bulk suspension. For viscous suspensions (and thus in the SBM), considering bulk and particle phase equations happens to be more convenient.

The averaged balance equations for the bulk suspension (i.e., the particles and fluid mixture) are

$$\nabla \cdot \mathbf{U} = 0, \tag{A1}$$

$$\nabla \cdot \boldsymbol{\Sigma} + \rho \mathbf{g} = 0, \tag{A2}$$

where $\mathbf{U} = \phi \mathbf{u}^{\mathrm{p}} + (1-\phi)\mathbf{u}^{\mathrm{f}}$ is the volume-averaged velocity of the suspension and $\mathbf{u}^{\mathrm{p}}$ and $\mathbf{u}^{\mathrm{f}}$ the local mean particle and fluid velocities, respectively. The density of the suspension is $\rho = \phi\rho_{\mathrm{p}} + (1-\phi)\rho_{\mathrm{f}}$ where ρ_{p} and ρ_{f} are the particle and fluid density, respectively. The bulk average suspension stress is noted $\boldsymbol{\Sigma}$. It is worth mentioning that the contribution to $\boldsymbol{\Sigma}$ due to the presence of the particles (often called the Batchelor stress[15]) contains (i) a hydrodynamic part (hydrodynamic stresslet and higher multipoles) and (ii) a non-hydrodynamic part linked to the direct interparticle or contact forces (Irving-Kirkwood stress)[19,20].

The averaged particle mass conservation equation yields

$$\frac{\partial \phi}{\partial t} + \nabla \cdot (\phi \mathbf{u}^{\mathrm{p}}) = 0, \tag{A3}$$

which, using the incompressibility of the bulk suspension (Eq. (A1)), can be rewritten

$$\frac{\partial \phi}{\partial t} + \mathbf{U} \cdot \nabla \phi = -\nabla \cdot \phi(\mathbf{u}^{\mathrm{p}} - \mathbf{U}), \tag{A4}$$

which exhibits the migration flux $\phi(\mathbf{u}^{\mathrm{p}} - \mathbf{U})$.

The averaging process performed on the particle phase gives a particle momentum equation of the form

$$\nabla \cdot \boldsymbol{\sigma}^{\mathrm{p}} + n\langle \mathbf{f}^{h} \rangle^{\mathrm{p}}_{\mathrm{drag}} + (\rho_{\mathrm{p}} - \rho_{\mathrm{f}})\phi\, \mathbf{g} = 0. \tag{A5}$$

where $\boldsymbol{\sigma}^{\mathrm{p}}$ comprises hydrodynamic and contact (or interparticle force) contributions. This later contact stress involved in $\boldsymbol{\sigma}^{\mathrm{p}}$ is identical to that included in $\boldsymbol{\Sigma}$. The hydrodynamic part involved in $\boldsymbol{\sigma}^{\mathrm{p}}$ is more difficult to grasp, as it comes from the non-drag part of the interphase hydrodynamic force and differs from the hydrodynamic part of the particle contribution to $\boldsymbol{\Sigma}$[19,20]. The drag part of the interphase force, $n\langle \mathbf{f}^h \rangle^{\mathrm{p}}_{\mathrm{drag}}$, can be written for spherical particles of diameter d as

$$n\langle \mathbf{f}^h \rangle^{\mathrm{p}}_{\mathrm{drag}} = -\frac{18\eta_{\mathrm{f}}}{d^2}\frac{\phi}{f(\phi)}(\mathbf{u}^{\mathrm{p}} - \mathbf{U}), \tag{A6}$$

with the empirical hindered settling function $f(\phi) = (1-\phi)^n$ (with $n \simeq 5$ at low Reynolds numbers) proposed by Richardson and Zaki[50]. The non-drag part of the interphase force, $n\langle \mathbf{f}^h \rangle^{\mathrm{p}}_{\mathrm{non-drag}}$, is related to forces acting on the particles and involving their concentration gradient or the gradient of the shear rate and can be written in the phenomenological form[19]

$$n\langle \mathbf{f}^h \rangle^{\mathrm{p}}_{\mathrm{non-drag}\,i} = -\eta_{\mathrm{f}}\phi\,\dot{\gamma} D_{ij}\frac{\partial \phi}{\partial x_j} + \eta_{\mathrm{f}}\phi B_{ijkl}\frac{\partial^2 u_l}{\partial x_j \partial x_k}. \tag{A7}$$

This non-drag portion can be also written as the divergence of a hydrodynamic stress[20] and is consequently included in $\boldsymbol{\sigma}^{\mathrm{p}}$ in Eq. (A5).

For neutrally buoyant particles, $\rho = \rho_{\mathrm{p}} = \rho_{\mathrm{f}}$, the momentum equation (A5) together with the expression for the drag (Eq. (A6)) provide the migration flux

$$\phi(\mathbf{u}^{\mathrm{p}} - \mathbf{u}) = \frac{d^2 f(\phi)}{18\eta_{\mathrm{f}}}\nabla \cdot \boldsymbol{\sigma}^{\mathrm{p}}. \tag{A8}$$

Particle migration is driven by the divergence of the normal component of the particle phase stress. As mentioned in Sec. I, there are experimental measurements of the normal stress of the particle phase, but it is unclear whether they are able to capture thoroughly the hydrodynamic and contact portions. These measurements, mostly done behind a grid, probably grab only the contact contribution. The proposed expressions for the normal viscosity may then miss the hydrodynamic component and may be only valid at large ϕ for which contact interactions prevail. In addition, these rheology experiments performed for uniform suspensions in a steady state are unlikely to apprehend forces acting on the particles involving gradients such as given by the phenomenological expression (A7). It may thus be necessary to add terms of that type to the usual rheological constitutive laws of Morris and Boulay[18] or of Boyer, Guazzelli, and Pouliquen[32].

In the cylindrical Couette geometry, when using the phenomenological expressions (3) and (5) introduced in Sec. I, the migration equation given by Eqs. (A4) and (A8) becomes

$$\frac{\partial \phi}{\partial t} = \frac{d^2}{18}\frac{\partial}{r\partial r}\left[r(1-\phi)^n \frac{\partial \eta_{\mathrm{n}}\dot{\gamma}}{\partial r}\right], \tag{A9}$$

in the absence of any additional forces such as the phenomenological forces of Eq. (A7); this is the most common migration equation found in the literature[18]. When a force due to a concentration gradient of the form of the first term of Eq. (A7) is included, the migration equation becomes

$$\frac{\partial \phi}{\partial t} = \frac{d^2}{18}\frac{\partial}{r\partial r}\left[r(1-\phi)^n\left(\frac{\partial \eta_n \dot{\gamma}}{\partial r} + D_{12}\dot{\gamma}\phi\frac{\partial \phi}{\partial r}\right)\right], \tag{A10}$$

where D_{12} is a dimensionless diffusion coefficient; Eq. (A9) is recovered with $D_{12} = 0$. The shear rate $\dot{\gamma}$ is obtained by solving the suspension momentum equation across the Couette gap:

$$\frac{d}{dr}(r^2 \eta_s \dot{\gamma}) = 0, \tag{A11}$$

which gives

$$\eta_s \dot{\gamma} = -\frac{\Omega}{r^2}\left[\int_{R_i}^{R_o} dr/\eta_s r^3\right]^{-1}, \tag{A12}$$

where Ω is the rotational speed of the inner cylinder. Moreover, the cross-stream migration flux has to be null at the inner and outer boundary, i.e., at $r = R_i$ and $r = R_o$.

In dimensionless form (using R_i as the length scale and ω^{-1} as the timescale), Eq. (A10) becomes

$$\frac{\partial \phi}{\partial \hat{t}} = \frac{d^2}{18R_i^2}\frac{\partial}{\hat{r}\partial \hat{r}}\left[\hat{r}(1-\phi)^n\left(\frac{\partial \eta_n \hat{\dot{\gamma}}}{\partial \hat{r}} + D_{12}\hat{\dot{\gamma}}\phi\frac{\partial \phi}{\partial \hat{r}}\right)\right], \tag{A13}$$

with the dimensionless shear rate $\hat{\dot{\gamma}}$ given by

$$\eta_s \hat{\dot{\gamma}} = -\frac{1}{\hat{r}^2}\left[\int_1^{R_o/R_i} d\hat{r}/\eta_s \hat{r}^3\right]^{-1}. \tag{A14}$$

To solve these equations, we need to choose rheological laws for η_s and η_n. In this paper, we have tested three cases, as described in Sec. IV:

(i) $\eta_s(\phi)$ and $\mu(\phi)$ given by Eqs. (13) and (14), as derived from the steady-state profiles in Sec. III A 2, with no diffusion term, i.e., $D_{12} = 0$ in Eq. (A10).

(ii) Eq. (B3) for $\mu(\phi)$ and Eq. (13) for $\eta_s(\phi)$ (this set of equations is a slightly modified form of the Boyer, Guazzelli, and Pouliquen[32] model). Eq. (B3) is consistent with direct measurements of the particle stresses for our suspensions (see Sec. II A, Fig. 7) and *a priori* accounts for contact forces only. $D_{12}(\phi)$ is here set as a free parameter, which *a priori* depends on ϕ, to account for possible hydrodynamic forces.

(iii) The same model is used as in (ii), but with the usual assumption $D_{12} = 0$ in the SBM for comparison.

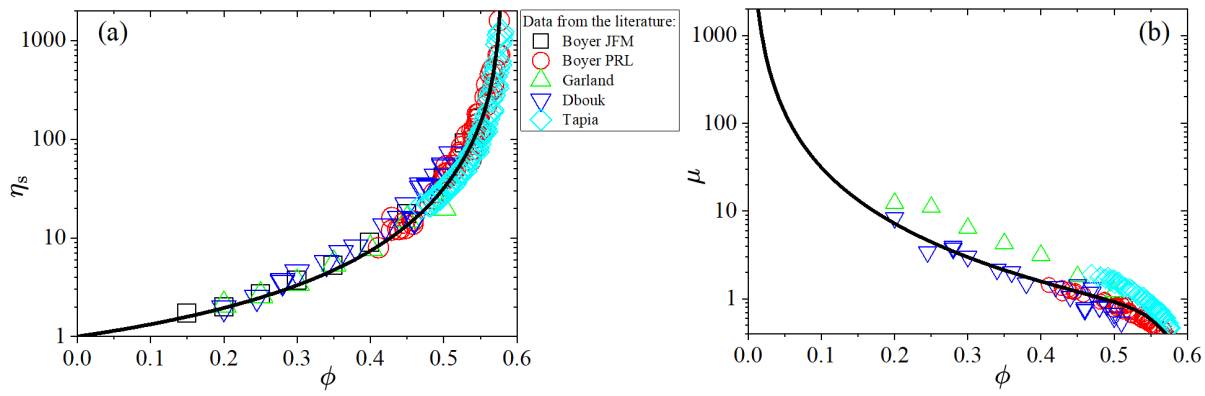

FIG. 7. Macroscopic measurements from the literature by Dbouk, Lobry, and Lemaire [30], Garland *et al.* [31], Boyer, Guazzelli, and Pouliquen [32], Tapia, Pouliquen, and Guazzelli [34], Boyer, Pouliquen, and Guazzelli [37] (see legend). (a) Dimensionless viscosity η_s, and (b) friction coefficient μ as a function of volume fraction ϕ. The lines are the rheological laws – Eqs. (B1), (B2) and (B3) – of Boyer, Guazzelli, and Pouliquen [32].

In the three cases, the exponent of the Richardson-Zaki correlation is taken to be $n = 5$. The steady-state volume fraction profile $\phi(r)$ for (i) and (iii) is easily computed as

$$\frac{\eta_n(\phi(r))}{\eta_s(\phi(r))} = \frac{1}{\mu(\phi(r))} = A\,r^2, \tag{A15}$$

where the proportionality factor A is obtained by ensuring mass conservation. There is no analytical solution for the dynamics of ϕ. The equations are thus solved numerically with an ordinary differential equation solver.

Appendix B: Macroscopic data from the literature

Macroscopic data from the literature on systems similar to ours (described in Sec. II A) are displayed in Fig. 7. Altogether, they provide a full macroscopic characterization of our system in the whole range of volume fraction, from the semi-dilute regime to the dense regime. All the viscosity data collapse quite well, whereas there is some scatter on the friction coefficient data. This points to the specific difficulty of performing particle normal stress measurements; it might be due to the differences in the geometries that are used and in the way particle stress is obtained as mentioned in Sec. I.

Boyer, Guazzelli, and Pouliquen [32] have proposed the following functions to describe the rheology of these suspensions:

$$\eta_s(\phi) = 1 + (5/2)\phi(1-\phi/\phi_j)^{-1} + \mu^c(\phi)(\phi/\phi_j)^2(1-\phi/\phi_j)^{-2} \quad \text{(B1)}$$

$$\eta_n(\phi) = (\phi/\phi_j)^2(1-\phi/\phi_j)^{-2} \quad \text{(B2)}$$

$$\mu(\phi) = \frac{\eta_s(\phi)}{\eta_n(\phi)} = \mu^c(\phi) + (5/2)\phi_j(\phi/\phi_j)^{-1}(1-\phi/\phi_j) + (\phi/\phi_j)^{-2}(1-\phi/\phi_j)^2 \quad \text{(B3)}$$

with $\phi_j = 0.585$, $\mu^c(\phi) = \mu_1 + (\mu_2-\mu_1)/[1+I_0\phi^2(\phi_j-\phi)^{-2}]$ and $\mu_1 = 0.32, \mu_2 = 0.7, I_0 = 0.005$. These expressions yield a fair fit to all the viscosity data, as well as to the friction coefficient measured by Boyer, Guazzelli, and Pouliquen [32] and Dbouk, Lobry, and Lemaire [30].

It should be noted that suspensions prepared with PEG show only very weak shear thinning[7,30,32,37], which makes the analysis of the data easier. This contrasts with suspensions of PS particles in silicone oil where strong shear thinning is observed[6,7], which implies to use a shear-stress-dependent ϕ_j in the modeling. In this last case, shear thinning is consistent with the observed decrease of the interparticle friction coefficient with the normal force[6,7] in the relevant range of normal forces. In PEG, the interparticle friction coefficient does not vary significantly with the normal force[7]. In our study, we can finally consider ϕ_j as a constant. This is confirmed by our experiments, where we have observed that changing the overall shear rate by up to two orders of magnitude does not affect the observed behavior.

Appendix C: Detailed analysis of the behavior of a 40% suspension

In this appendix, we detail the results obtained for a 40% volume fraction suspension. We show how the step by step analysis of the data is performed to extract information on the volume fraction dependence of the suspension viscosity and friction coefficient, and to compare the observed dynamics of migration with the SBM. Similar analysis has been performed for all studied volume fractions.

In Fig. 8, we plot the initial and steady-state velocity and volume fraction profiles. Initially, the loaded suspension is homogeneous. Consistently, the initial velocity profile is well fitted to a Newtonian velocity profile. The steady-state volume fraction profile shows strong shear-induced migration from the inner cylinder to the outer cylinder, the volume fraction varying from 36% close to the inner cylinder to 42% close to the outer cylinder.

From the steady-state velocity profiles, the steady-state shear rate profile can be computed.

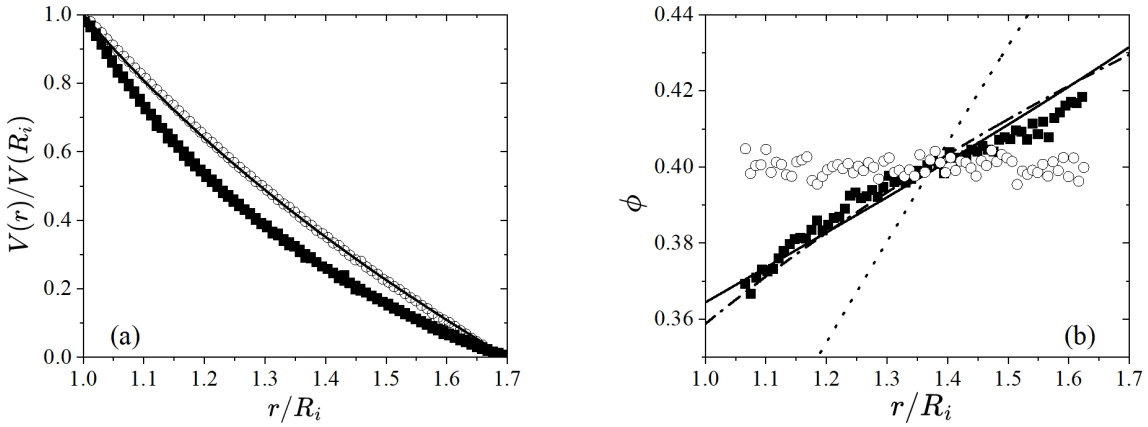

FIG. 8. Initial (empty circles) and steady (squares) velocity (a) and concentration (b) profiles for a 40% suspension. The full line in (a) is the theoretical velocity profile for a homogeneous Newtonian fluid. The lines in (b) are the predictions of the SBM with the three sets of equations described in Sec. IV [(i): dashed-dotted line, (ii): solid line, and (iii): dotted line].

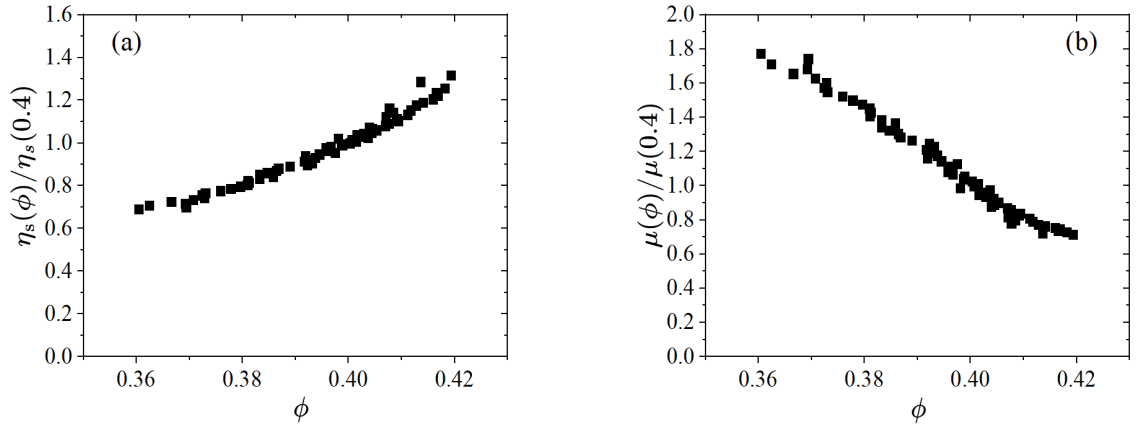

FIG. 9. Local variation of the viscosity (a) and of the friction coefficient (b) as a function of the local volume fraction for a 40% suspension.

When it is combined with the steady-state volume fraction profile, as detailed in Sec. II B, the relative variation of the viscosity with volume fraction can be derived as $\eta_s(\phi(r))/\eta_s(\phi(R_1)) = (R_1^2/r^2) \times (\dot{\gamma}(r)/\dot{\gamma}(R_1))$, which is plotted in Fig. 9a. In this plot, the reference viscosity $\eta_s(\phi(R_1))$ is taken to be that at a 40% volume fraction. It is observed that the viscosity varies by a factor of order 2 from 36% to 42%, which is consistent with the observations of the literature (Fig. 7).

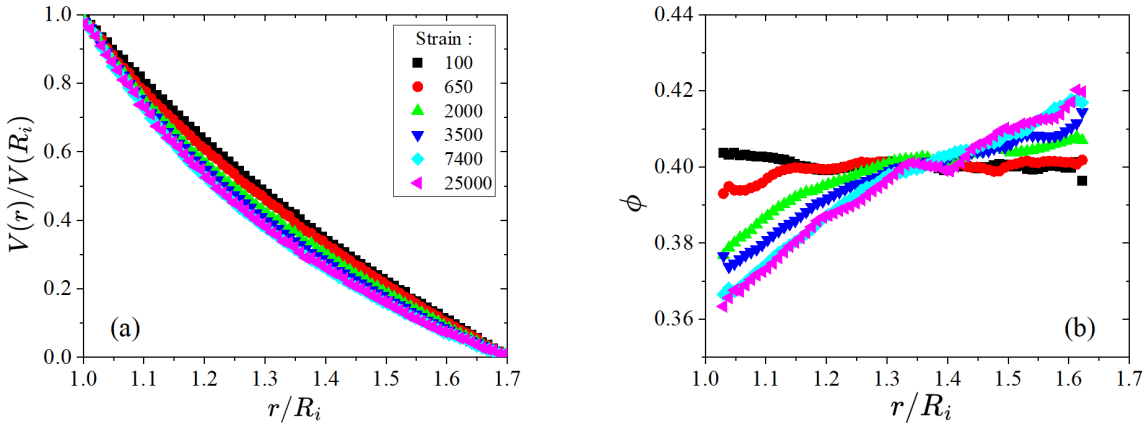

FIG. 10. Evolution of the velocity (a) and concentration (b) profiles as a function of the macroscopic strain $\Gamma = \Omega t$ (see legend) for a 40% suspension. The concentration profiles are computed here from the velocity profiles, as described in the text.

From the steady-state volume fraction profiles, as detailed in Sec. II B, *in the absence of a diffusion term of hydrodynamic origin in the migration equation* (A10) *of the SBM*, the variation of the friction coefficient with volume fraction can be derived as $\mu(\phi(r))/\mu(\phi(R_1)) = R_1^2/r^2$, which is plotted in Fig. 9b. In this plot, the reference friction coefficient $\mu(\phi(R_1))$ is taken to be that at a 40% volume fraction. It is observed to decrease by a factor of order 2.5 from 36% to 42%, which is much higher than the factor 1.4 observed in the literature (see Fig. 7). This is commented in the main text.

As explained in Sec. II B, these relative variations of the viscosity and of the friction coefficient can be converted into quantitative data, provided their value at a given volume fraction is known.

We now turn to the examination of the migration dynamics. In Fig. 10a we plot the velocity profiles as a function of the macroscopic strain. It is observed that the velocity profiles are more and more curved, and that a steady-state is reached after a strain of order 7000. The progressive curvature of the velocity profiles is the signature of the increase of the ratio between the velocity gradient close to the inner cylinder and that close to the outer cylinder. Initially, on the homogeneous material, this ratio is the same as the stress ratio, R_o^2/R_i^2 (Eq. (8)); for inhomogeneous material, this ratio is increased by a factor $\eta_s(\phi(R_o))/\eta_s(\phi(R_i))$ (Eq. (10)). The curvature of $V(r)$ is thus the signature of the progressive shear-induced migration from the inner cylinder to the outer cylinder. Accordingly, the maximal velocity variation within the gap of the geometry is observed

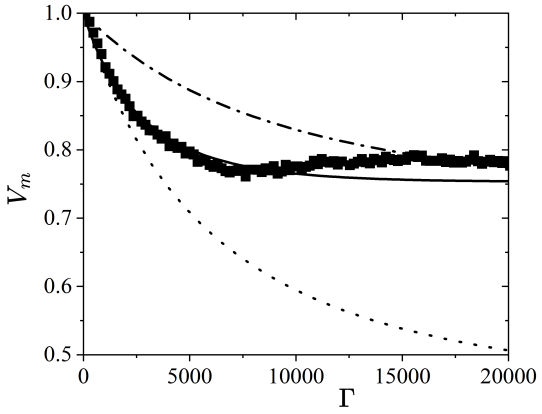

FIG. 11. Evolution of the velocity V_m in the middle of the gap as a function of the macroscopic strain $\Gamma = \Omega t$ for a 40% suspension: experimental data (squares) and predictions of the SBM (lines) with the three sets of equations described in Sec. IV [(i): dashed-dotted line, (ii): solid line, and (iii): dotted line].

close to the middle of the gap. The velocity evolution with strain at this position is plotted in Fig. 11. It clearly illustrates migration and shows that migration stops after a strain of order 7000. The evolution of the velocity as a function of strain can be compared to the prediction of the SBM, which is done in detail in Sec. IV (these predictions are shown in Fig. 11).

These velocity profiles are sufficient to study the dynamics of migration and to test the SBM. However, it may seem interesting to examine the volume-fraction-profile time evolution. Once the local viscosity evolution with volume fraction has been computed from steady-state profiles, the analysis can be reversed on the transient velocity profiles: from each profile, a shear rate profile can be extracted, and then the relative variation of the viscosity within the gap can be computed. Then, inverting the $\eta_s(\phi)$ function gives access to the volume fraction profiles in time. In the absence of information on the torque, this problem does not have a unique solution, since only relative variations are known. However, a unique volume fraction profile is finally obtained by guaranteeing mass conservation. The result of this analysis is displayed in Fig. 10b.

To show better the migration dynamics and to compare it to existing models, it is convenient to plot the local volume fraction evolution with the macroscopic strain at several positions. These evolutions, close to the inner cylinder, close to the outer cylinder, and in the middle of the gap, are shown in Fig. 12, together with the predictions of the SBM with the three sets of equations described in Sec. IV. The same conclusions are reached as when studying the SBM prediction

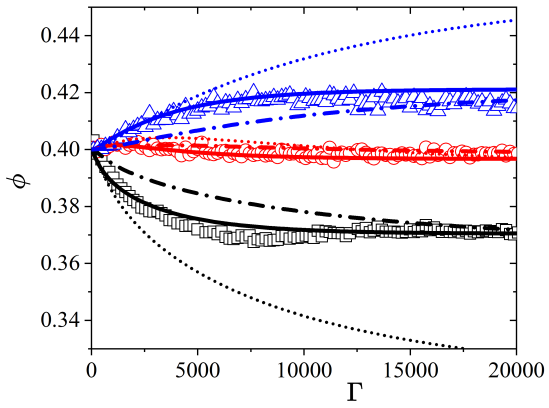

FIG. 12. Evolution of the local volume fraction as a function of the macroscopic strain $\Gamma = \Omega t$ for a 40% suspension, at various dimensionless radial positions r/R_i in the gap of the Couette geometry: experimental data (symbols) and predictions of the SBM (lines) with the three sets of equations described in Sec. IV [(i): dashed-dotted line, (ii): solid line, and (iii): dotted line]. Data are taken at $r/R_i = 1.07$ (black lines and squares), $r/R_i = 1.35$ (red lines and circles) and $r/R_i = 1.6$ (blue lines and triangles); we recall that the outer wall location is $R_o/R_i = 1.7$. The local concentrations are computed here from the velocity profiles, as described in the text.

for the steady-state volume fraction profile and the evolution of the velocity vs. strain: model (i), based on a local estimate of $\mu(\phi)$, provides a good match with the magnitude of migration, but its dynamics is too slow; with model (iii), based on the macroscopic $\mu(\phi)$, the magnitude of the predicted migration is too high and its dynamics is too slow; good agreement with both the magnitude and the dynamics of migration is finally obtained with model (ii), which accounts for an additional diffusive term in the SBM.

It should be noted that volume fraction profiles inferred from velocity profiles are more noisy than the velocity profiles since they are based on their derivative; in particular, at low volume fraction, volume fraction changes are hardly detectable, whereas velocity variations are clearly observed. In the rest of the paper, this analysis in terms of local volume fraction evolution is thus not shown as it cannot be performed systematically; we focus on the velocity profiles evolution, which provides all the required information to analyze the migration dynamics.

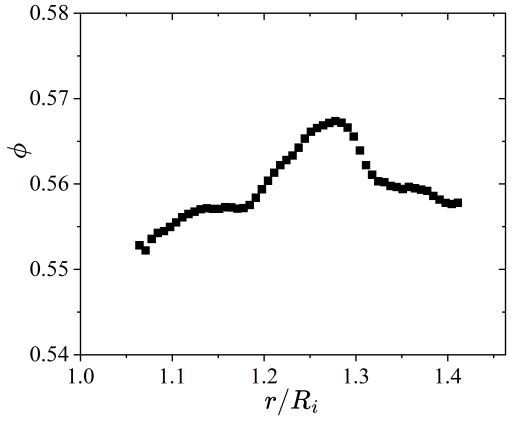

FIG. 13. Initial volume fraction profile (after loading) of a 56% suspension in a wide gap Couette geometry of inner radius 4.1 cm and outer radius 6 cm, slightly different from that used in the rest of the paper.

Appendix D: Initial state of a 56% suspension

In Fig. 13, we plot the volume fraction profile after loading a 56% suspension in a wide-gap Couette geometry (of inner radius 4.1 cm and outer radius 6 cm, slightly different from that used in the rest of the paper). Loading consists in pouring the material in the cup (outer cylinder), and in inserting the bob (inner cylinder) in the cup.

We observe that the loaded material is inhomogeneous: there is an accumulation of particles in the middle of the gap. It is likely due to the fact that the insertion of the bob induces a shear flow in the annular channel between the bob and the cup walls, the vertical direction being the flow direction, and the radial direction the velocity gradient direction. In such configuration, the shear rate during the loading is maximal near both walls, leading to shear-induced migration towards the middle of the gap. From the geometry dimensions, the shear strain experienced by the suspension during the loading can be estimated as being of order ten. The fact that migration happens for such low strain is consistent with the value $\Gamma_{1/2} = 100$ found for $\phi = 54.5\%$ in Sec. III B and with the dynamics of migration being dramatically faster with increasing particle volume fraction at the approach of jamming. It shows the difficulty in studying highly concentrated suspensions and in obtaining reliable results on such materials. To avoid migration during loading, a possibility would be to use a wide-gap vane-in-cup geometry; however, other difficulties arise with these geometries, since (i) flow is actually 2D in this geometry, and (ii) there is particle depletion near the vane blades[51].

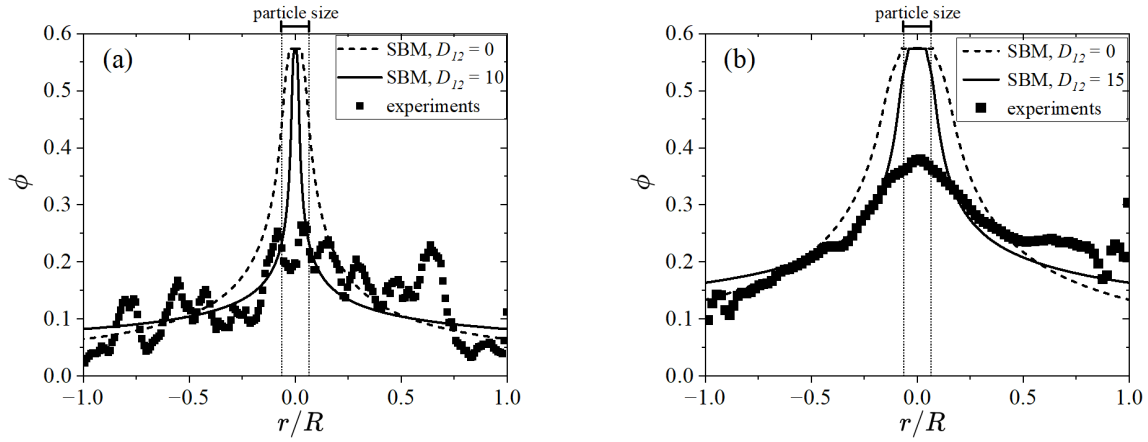

FIG. 14. Steady-state volume fraction profiles in a pipe geometry for (a) a 10% and (b) a 20% suspension. Squares: experimental results of Snook, Butler, and Guazzelli[27]. Dashed line, SBM prediction for $D_{12} = 0$. Full line, SBM prediction for the D_{12} values found in the present paper ($D_{12} = 10$ for $\phi = 10\%$ and $D_{12} = 15$ for $\phi = 15\%$). The bar and the vertical dotted lines indicate the particle size.

Appendix E: Predictions for a Poiseuille flow

We have solved the SBM for a Poiseuille flow, as described in Ref. 27, with an additional concentration gradient term. More precisely, we have used the model (ii) described in Sec. IV, which accounts quantitatively for both the dynamics and the steady state of migration in the Couette cell. We recall that it consists of Eq. (B3) for $\mu(\phi)$ and Eq. (13) for $\eta_s(\phi)$, together with $D_{12} \neq 0$ in Eq. (A7) to account for a possible term of hydrodynamic origin in the stress driving migration.

In Fig. 14, we present the steady-state volume fraction profiles observed experimentally by Snook, Butler, and Guazzelli[27] for a 10% and a 20% suspension. These experiments have been performed on a suspension of PMMA particles of diameter $a = 1.05$ mm in a water/$ZnCl_2$/Triton X-100 mixture, in a pipe of radius $R = 8.25$ mm. The observations are compared to the predictions of the SBM in the case $D_{12} = 0$ (standard SBM), as well as in the cases $D_{12} = 10$ for $\phi = 10\%$ and $D_{12} = 15$ for $\phi = 20\%$ (as found here for the Couette flow).

A remarkable result of Ref. 27 is the limited migration as compared to that predicted by the standard SBM for a 20% suspension. In particular, the concentration is found to increase up to 40% only in the central region whereas the model predicts that it should reach ϕ_j (Fig. 14b). By contrast with the SBM with $D_{12} = 0$, the SBM with $D_{12} = 15$ provides a good agreement with the experimental data for radial positions r/R in the pipe $1 < r/R < 0.15$. Since the particle diameter

is $a = 0.13R$, it can then be hypothesized that the volume fraction saturation at $\phi \simeq 35\%$ in the central region $0.15 < r/R$ is a finite size effect which cannot be captured by a continuum modeling. Indeed, although the SBM with $D_{12} = 15$ still predicts that ϕ should theoretically reach ϕ_j at the center, the size of the region where $\phi = \phi_j$ is predicted to be narrower than the particle size in the experiment, which does not make sense. The volume fraction predicted at a distance of one particle diameter from the center is actually 38%, which is in fair agreement with the value found in the experiment in the central region.

Another remarkable results from Ref. 27 is the absence of any significant migration for a 10% suspension, which is reminiscent of our results in the Couette cell. As observed in Fig. 14a, the model with $D_{12} = 10$ (as found here) predicts significant migration in a very narrow region in the pipe center, of size much lower than the particle diameter; e.g., a volume fraction larger than 20% is predicted only for $0.09 > r/R$, that is for radial positions smaller than one particle diameter. By contrast, the model with $D_{12} = 0$ predicts that $\phi > 20\%$ for any position in the range $0.2 > r/R$, which would in principle lead to observable migration. Therefore, again, the model with a diffusive term is found to be consistent with the observations.

These first results are promising. In order to make a strong conclusion, the experiments now have to be conducted in a pipe with the same system as in the Couette cell (PS particles in PEG), with an in-depth investigation of the migration dynamics.

ACKNOWLEDGMENTS

The nuclear magnetic resonance experiments have been performed at Laboratoire Navier.

REFERENCES

[1]J. F. Guazzelli, É. andMorris, *A Physical Introduction to Suspension Dynamics* (Cambridge University Press, 2012).

[2]M. M. Denn and J. F. Morris, "Rheology of non-brownian suspensions," Annual Review of Chemical and Biomolecular Engineering **5**, 203–228 (2014).

[3]É. Guazzelli and O. Pouliquen, "Rheology of dense granular suspensions," Journal of Fluid Mechanics **852**, P1 (2018).

[4]G. Chatté, J. Comtet, A. Niguès, L. Bocquet, A. Siria, G. Ducouret, F. Lequeux, N. Lenoir, G. Ovarlez, and A. Colin, "Shear thinning in non-brownian suspensions," Soft matter **14**, 879–893 (2018).

[5]L. Lobry, E. Lemaire, F. Blanc, S. Gallier, and F. Peters, "Shear thinning in non-brownian suspensions explained by variable friction between particles," Journal of Fluid Mechanics **860**, 682–710 (2019).

[6]M. Arshad, A. Maali, C. Claudet, L. Lobry, F. Peters, and E. Lemaire, "An experimental study on the role of inter-particle friction in the shear-thinning behavior of non-brownian suspensions," Soft Matter **17**, 6088–6097 (2021).

[7]A. V. N. Le, A. Izzet, G. Ovarlez, and A. Colin, "Solvents govern rheology and jamming of polymeric bead suspensions," Journal of Colloid and Interface Science **629**, 438–450 (2023).

[8]R. Mari, R. Seto, J. F. Morris, and M. M. Denn, "Shear thickening, frictionless and frictional rheologies in non-brownian suspensions," Journal of Rheology **58**, 1693–1724 (2014).

[9]M. Wyart and M. E. Cates, "Discontinuous shear thickening without inertia in dense non-brownian suspensions," Physical Review Letters **112**, 098302 (2014).

[10]N. Y. Lin, B. M. Guy, M. Hermes, C. Ness, J. Sun, W. C. Poon, and I. Cohen, "Hydrodynamic and contact contributions to continuous shear thickening in colloidal suspensions," Physical Review Letters **115**, 228304 (2015).

[11]J. Comtet, G. Chatté, A. Niguès, L. Bocquet, A. Siria, and A. Colin, "Pairwise frictional profile between particles determines discontinuous shear thickening transition in non-colloidal suspensions," Nature communications **8**, 1–7 (2017).

[12]J. F. Morris, "Shear thickening of concentrated suspensions: Recent developments and relation to other phenomena," Annual Review of Fluid Mechanics **52**, 121–144 (2020).

[13]J. F. Morris, "A review of microstructure in concentrated suspensions and its implications for rheology and bulk flow," Rheologica Acta **48**, 909–923 (2009).

[14]F. Blanc, E. Lemaire, A. Meunier, and F. Peters, "Microstructure in sheared non-brownian concentrated suspensions," Journal of Rheology **57**, 273–292 (2013).

[15]G. Batchelor, "The stress system in a suspension of force-free particles," JJournal of Fluid Mechanics **41**, 545–570 (1970).

[16]S. Gallier, E. Lemaire, F. Peters, and L. Lobry, "Rheology of sheared suspensions of rough frictional particles," Journal of Fluid Mechanics **757**, 514–549 (2014).

[17]P. R. Nott and J. Brady, "Pressure-driven flow of suspensions: simulation and theory," Journal of Fluid Mechanics **275**, 157–199 (1994).

[18]J. Morris and F. Boulay, "Curvilinear flows of noncolloidal suspensions: The role of normal stresses," Journal of Rheology **43**, 1213–1237 (1999).

[19]D. Lhuillier, "Migration of rigid particles in non-Brownian viscous suspensions," Phys. Fluids **21**, 023302 (2009).

[20]P. R. Nott, É. Guazzelli, and O. Pouliquen, "The suspension balance model revisited," Phys. Fluids **23**, 043304 (2011).

[21]J. Abbott, N. Tetlow, A. Graham, S. Altobelli, E. Fukushima, L. Mondy, and T. Stephens, "Experimental observations of particle migration in concentrated suspensions: Couette flow," Journal of Rheology **35**, 773–795 (1991).

[22]N. Tetlow, A. L. Graham, M. S. Ingber, S. R. Subia, L. A. Mondy, and S. A. Altobelli, "Particle migration in a couette apparatus: Experiment and modeling," Journal of Rheology **42**, 307–327 (1998).

[23]G. Ovarlez, F. Bertrand, and S. Rodts, "Local determination of the constitutive law of a dense suspension of noncolloidal particles through magnetic resonance imaging," Journal of Rheology **50**, 259–292 (2006).

[24]M. Sarabian, M. Firouznia, B. Metzger, and S. Hormozi, "Fully developed and transient concentration profiles of particulate suspensions sheared in a cylindrical couette cell," Journal of Fluid Mechanics **862**, 659–671 (2019).

[25]C. J. Koh, P. Hookham, and L. G. Leal, "An experimental investigation of concentrated suspension flows in a rectangular channel," Journal of Fluid Mechanics **266**, 1–32 (1994).

[26]M. K. Lyon and L. G. Leal, "An experimental study of the motion of concentrated suspensions in two-dimensional channel flow. Part 1. Monodisperse systems," Journal of Fluid Mechanics **363**, 25–56 (1998).

[27]B. Snook, J. E. Butler, and É. Guazzelli, "Dynamics of shear-induced migration of spherical particles in oscillatory pipe flow," Journal of Fluid Mechanics **786**, 128–153 (2016).

[28]S. Altobelli, E. Fukushima, and L. Mondy, "Nuclear magnetic resonance imaging of particle migration in suspensions undergoing extrusion," Journal of Rheology **41**, 1105–1115 (1997).

[29]A. Deboeuf, G. Gauthier, J. Martin, Y. Yurkovetsky, and J. F. Morris, "Particle pressure in a sheared suspension: A bridge from osmosis to granular dilatancy," Physical Review Letters **102**, 108301 (2009).

[30]T. Dbouk, L. Lobry, and E. Lemaire, "Normal stresses in concentrated non-Brownian suspensions," Journal of Fluid Mechanics **715**, 239–272 (2013).

[31]S. Garland, G. Gauthier, J. Martin, and J. F. Morris, "Normal stress measurements in sheared non-Brownian suspensions," Journal of Rheology **57**, 71–88 (2013).

[32]F. Boyer, É. Guazzelli, and O. Pouliquen, "Unifying Suspension and Granular Rheology," Physical Review Letters **107**, 188301 (2011).

[33]B. Etcheverry, Y. Forterre, and B. Metzger, "Capillary-stress controlled rheometer reveals the dual rheology of shear-thickening suspensions," Physical Review X **13**, 011024 (2023).

[34]F. Tapia, O. Pouliquen, and É. Guazzelli, "Influence of surface roughness on the rheology of immersed and dry frictional spheres," Physical Review Fluids **4**, 104302 (2019).

[35]E. d'Ambrosio, F. Blanc, and E. Lemaire, "The characterization of the particle normal stresses of concentrated granular suspensions by local rheometry," Journal of Fluid Mechanics **967**, A34 (2023).

[36]E. d'Ambrosio, F. Blanc, and E. Lemaire, "Viscous resuspension of non-brownian particles: determination of the concentration profiles and particle normal stresses," Journal of Fluid Mechanics **911**, A22 (2021).

[37]F. Boyer, O. Pouliquen, and É. Guazzelli, "Dense suspensions in rotating-rod flows: normal stresses and particle migration," Journal of Fluid Mechanics **686**, 5–25 (2011).

[38]J. Raynaud, P. Moucheront, J. Baudez, F. Bertrand, J. Guilbaud, and P. Coussot, "Direct determination by nuclear magnetic resonance of the thixotropic and yielding behavior of suspensions," Journal of Rheology **46**, 709–732 (2002).

[39]G. Ovarlez, S. Rodts, A. Ragouilliaux, P. Coussot, J. Goyon, and A. Colin, "Wide-gap couette flows of dense emulsions: Local concentration measurements, and comparison between macroscopic and local constitutive law measurements through magnetic resonance imaging," Physical Review E **78**, 036307 (2008).

[40]F. Blanc, F. Peters, and E. Lemaire, "Particle image velocimetry in concentrated suspensions: Application to local rheometry," Applied Rheology **21**, 23735 (2011).

[41]P. Coussot, *Rheometry of pastes, suspensions, and granular materials: applications in industry and environment* (John Wiley & Sons, 2005).

[42]P. T. Callaghan, *Principles of nuclear magnetic resonance microscopy* (Oxford University Press, 1991).

[43]P. T. Callaghan, "Rheo-nmr: nuclear magnetic resonance and the rheology of complex fluids," Reports on Progress in Physics **62**, 599 (1999).

[44]S. Rodts, F. Bertrand, S. Jarny, P. Poullain, and P. Moucheront, "Développements récents dans l'application de l'irm à la rhéologie et à la mécanique des fluides," Comptes Rendus Chimie **7**, 275–282 (2004).

[45]S. Rodts, J. Boujlel, B. Rabideau, G. Ovarlez, N. Roussel, P. Moucheront, C. Lanos, F. Bertrand, and P. Coussot, "Solid-liquid transition and rejuvenation similarities in complex flows of thixotropic materials studied by nmr and mri," Physical Review E **81**, 021402 (2010).

[46]A. Fall, A. Lemaître, F. Bertrand, D. Bonn, and G. Ovarlez, "Shear Thickening and Migration in Granular Suspensions," Physical Review Letters **105**, 268303 (2010).

[47]G. Ovarlez, F. Mahaut, S. Deboeuf, N. Lenoir, S. Hormozi, and X. Chateau, "Flows of suspensions of particles in yield stress fluids," Journal of Rheology **59**, 1449–1486 (2015).

[48]D. A. Drew, "Mathematical modeling of two-phase flow," Annual Review of Fluid Mechanics **15**, 261–291 (1983).

[49]R. Jackson, "Locally averaged equations of motion for a mixture of identical spherical particles and a newtonian fluid," Chemical Engineering Science **52**, 2457–2469 (1997).

[50]J. Richardson and W. Zaki, "The sedimentation of a suspension of uniform spheres under conditions of viscous flow," Chemical Engineering Science **3**, 65–73 (1954).

[51]G. Ovarlez, F. Mahaut, F. Bertrand, and X. Chateau, "Flows and heterogeneities with a vane tool: Magnetic resonance imaging measurements," Journal of Rheology **55**, 197–223 (2011).